Geomechanics and Engineering, *Vol. 37, No. 2 (2024) 149-166*
https://doi.org/10.12989/gae.2024.37.2.149

Acoustic emission characteristics under the influence of different stages of damage in granite specimens

Jong-Won Lee[1a], Tae-Min Oh*[2], Hyunwoo Kim[3b], Min-Jun Kim[4c] and Ki-Il Song[5d]

[1]*Research Institute of Industrial Technology, Pusan National University, 2 Busandaehak-ro 63beon-gil, Geumjeong-gu, Busan 46241, Republic of Korea*
[2]*Department of Civil and Environmental Engineering, Pusan National University, 2 Busandaehak-ro 63beon-gil, Geumjeong-gu, Busan 46241, Republic of Korea*
[3]*Mineral Exploration and Mining Research Center, Korea Institute of Geoscience and Mineral Resources (KIGAM), 124 Gwahang-no, Yuseong-gu, Daejeon 34132, Republic of Korea*
[4]*Deep Subsurface Storage & Disposal Research Center, Korea Institute of Geoscience and Mineral Resources (KIGAM), 124 Gwahang-no, Yuseong-gu, Daejeon 34132, Republic of Korea*
[5]*Department of Civil Engineering, Inha University, 100 Inha-ro, Michuhol-gu, Incheon 22212,Republic of Korea*

(*Received November 27, 2023, Revised March 18, 2024, Accepted March 31, 2024*)

Abstract. The acoustic emission (AE) technique is utilized to estimate the rock failure status in underground spaces. Understanding the AE characteristics under loading conditions is essential to ensure the reliability of AE monitoring. The AE characteristics depend on the material properties (p-wave velocity, density, UCS, and Young's modulus) and damage stages (stress ratio) of the target rock mass. In this study, two groups of granite specimens (based on the p-wave velocity regime) were prepared to explore the effect of material properties on AE characteristics. Uniaxial compressive loading tests with an AE measurement system were performed to investigate the effect of the rock properties using AE indices (count index, energy index, and amplitude index). The test results were analyzed according to three damage stages classified by the stress ratio of the specimens. Count index was determined to be the most suitable AE index for evaluating rock mass stability.

Keywords: acoustic emission; AE index; damage stages; rock properties

1. Introduction

Underground spaces have been broadly utilized to dispose of unwanted materials, such as high-level radioactive waste (HLW), because underground rock masses provide environmentally or socially isolated conditions (Costin 1997, Siren *et al*. 2015, Wang *et al*. 2018). The HLW repository is composed of a primary barrier (i.e., bentonite buffer) and a secondary barrier (i.e., surrounding rock mass) to restrain the release of radionuclides (Kim *et al*. 2018). In particular, granite rock materials that have low permeability and high strength are considered the primary target site of the HLW repository (Hudson *et al*. 2013). To protect the HLW during decay, the disposal site has been designed to operate in the underground space for more than ten thousand years (Fairhurst 2004, Zhang *et al*. 2020a). Therefore, monitoring the stability of rock masses during unexpected risks (e.g., earthquakes or decay heat) is essential.

To ensure the mechanical stability of a rock mass, non-destructive testing (NDT) methods have been applied to investigate the damage location or state of the rock mass. The NDT methods are used to inspect the status of materials without damage and are based on mechanical oscillation, radiation, optical, electric, and electro-magnetic (Howard 1991). Among them, the acoustic emission (AE) technique has been used to evaluate the damage location and damage level in rock engineering fields, as shown in Table 1. The AE technique uses elastic waves with a high-frequency band (5–500 kHz) generated by cracking inside a rock mass (Ishida *et al.* 2017). It is a valuable technique to monitor the stability of underground rock masses because the rock has limited accessibility for inspection compared with the surface (Fu and Tang 2021, Zhang *et al*. 2021).

AE characteristics depend on the mechanical properties (e.g., uniaxial compressive strength (UCS) and elastic modulus) and damage stages (e.g., crack development or energy conservation theory) of the rock mass. Considering the mechanical properties of the rock mass, the number of AE hits increases with a decrease in the UCS and Young's modulus under uniaxial compressive loading conditions (Petružálek *et al.* 2019, Wang *et al.* 2020). Since small-scale deformations mainly occur for specimens with low UCS and Young's modulus, a large number of AE hits are continuously generated for the rock specimens during the

*Corresponding author, Associate Professor
E-mail: geotaemin@pusan.ac.kr
[a]Ph.D., Post-Doctoral Researcher
E-mail: lee.j@pusan.ac.kr
[b]Ph.D., Principal Researcher
E-mail: hyunwoo.kim@kigam.re.kr
[c]Ph.D., Senior Researcher
E-mail: kimmj@kigam.re.kr
[d]Professor
E-mail: ksong@inha.ac.kr

ISSN: 2005-307X (Print), 2092-6219 (Online)

Fig. 1 Granite specimens for uniaxial compression test

Table 1 Literature review for AE application to investigate the behavior of rock mass

Reference	Test method	Evaluating characteristics with AE	Used AE parameters	Rock type
Aker *et al*. (2014)	*TCS	Source location	Arrival time	Sandstone
Stoeckhert *et al*. (2015)	TCS	Fluid injection, Cyclic loading, Source location	Amplitude	Sandstone
Lei *et al*. (2016)	TCS	Source location	Event, b-value	Granite
Gong *et al*. (2017)	TCS	Confining pressure	Frequency	Limestone
Cao *et al*. (2019)	**UCS	Loading rate	Event, Energy, Count, Amplitude, Peak frequency	Sandstone
Li *et al*. (2019)	UCS	Failure level, Source location	Count, Frequency	Sandstone
Meng *et al*. (2019)	Direct shear test	Shear rate	Event, Energy, b-value	Granite
Wang *et al*. (2019)	UCS, TCS	Energy conservation theory	Count, Energy, ASL, Amplitude	Limestone
Zhang *et al*. (2019)	UCS	Failure level, Source location	Event, Count, Energy, Frequency	Granite
Zhu *et al*. (2019)	UCS, Brazilian test	Temperature, Cyclic loading	Count	Granite
Zhang *et al*. 2020b	UCS	Failure level	Duration, Count, Energy, Amplitude, Frequency	Granite

*TCS: Triaxial compressive strength test, **UCS: Uniaxial compressive strength test

compressive loading process. In addition, b-value, which indicates the relationship between the amplitude and number of AE hits, increases with UCS under tensile loading conditions (Nejati and Ghazvinian 2014). These results indicate that large-scale fracture is greater in specimens with a higher UCS.

The AE characteristics are also influenced by the damage stages, such as damage level or deformation stage, with in the rock mass (Niu *et al*. 2023). When subjected to compressive loading conditions, rock specimens undergo a series of crack development stages, including initial crack closure, new crack generation, crack expansion, and ultimate failure (Nicksiar and Martin 2012, Xue *et al*. 2014). These distinct damage stages can be identified through the analysis of AE parameters, including hit, count, and the intensity of AE signals, particularly under compressive loading conditions.

Recent studies have highlighted the significance of AE parameters, such as hit, count, energy, and b-value, in delineating damage stages during compressive loading tests (Zhao *et al*. 2013, Kim *et al*. 2015, Li *et al*. 2022). However, previous research has primarily focused on investigating damage stages using AE parameters in relation to limited material properties, such as mechanical and physical properties, of the rock. It is important to note that variations in material properties can significantly affect strain behavior and crack occurrence in rocks, leading to diverse patterns of AE generation by cracking.

In this study, a uniaxial compressive test was performed with an AE system to analyze the AE characteristics according to the damage stage of the granite specimens. The granite specimens were classified into two groups based on the p-wave velocity. In addition, the AE characteristics

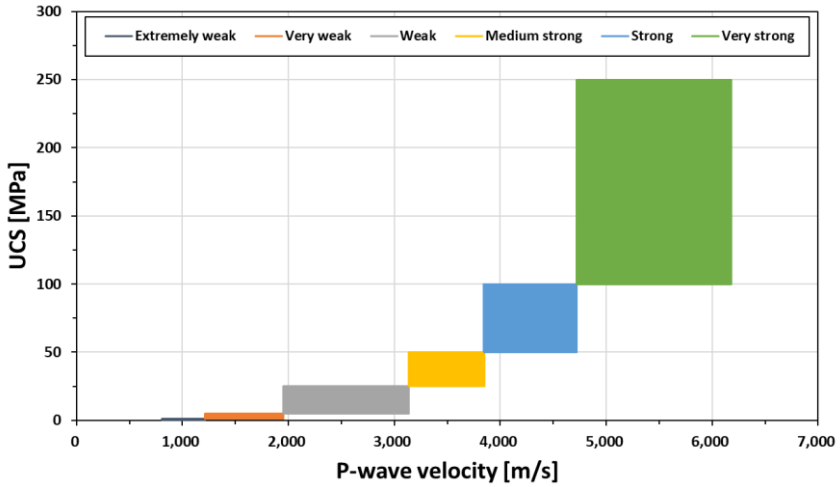

Fig. 2 ISRM classification of granite based on UCS and p-wave velocity (after Bieniawski and Bernede 1979)

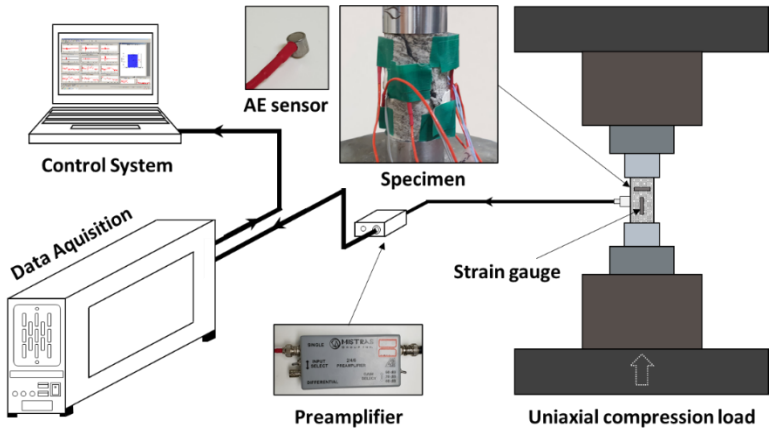

Fig. 3 Experimental setup for AE measurement during uniaxial compression test

Table 2 Material properties of specimens

Specimen	V_p [m/s]	ρ [g/cm^3]	UCS [MPa]	E [GPa]	Note
R1	2,416.7	2.62	18.8	3.49	
R2	2,669.0	2.62	64.5	12.81	Group A
R3	2,680.7	2.89	22.1	3.02	
R4	4,614.5	2.73	60.4	36.05	
R5	4,738.0	2.79	66.9	66.23	
R6	5,241.4	2.92	143.8	48.59	Group B
R7	5,637.8	3.06	102.0	60.36	
R8	5,833.3	2.92	142.6	53.34	

V_p: P-wave velocity, ρ: Density, UCS: Uniaxial Compressive Strength, E: Young's modulus

were considered as count index, energy index, and amplitude index to evaluate the damage stage according to rock properties (i.e., p-wave velocity, density, uniaxial compressive strength, and Young's modulus). Finally, an effective AE parameter was suggested to monitor the stability of granite, considering the damage stage with the stress ratio (applied stress per maximum strength). This study is expected to be useful for evaluating the damage to underground spaces with various rock properties of granite based on the AE technique.

.

2.2 Test setup and procedure

Fig. 3 shows the acoustic emission measurement system setup with uniaxial compressive loading. A uniaxial compressive test was performed with an AE system to investigate the AE characteristics according to the applied vertical stress. The loading rate was set to 0.1 mm/min to induce failure of the rock specimen within 15 minutes during the compressive loading test (ASTM 2002). Two strain gauges were installed to obtain the strain rate along the diameter and length directions on the surface of the specimen.

The acoustic emission measurement system consists of sensors, a pre-amplifier, a data acquisition system, and a system controller. The data acquisition and controller (Micro-II Express-Express 8 manufactured by Physical

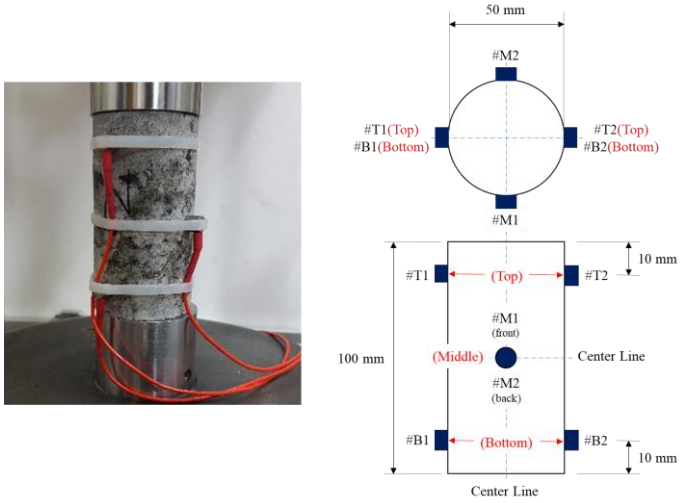

Fig. 4 Array configuration for sensor installation on the granite specimen during compression test

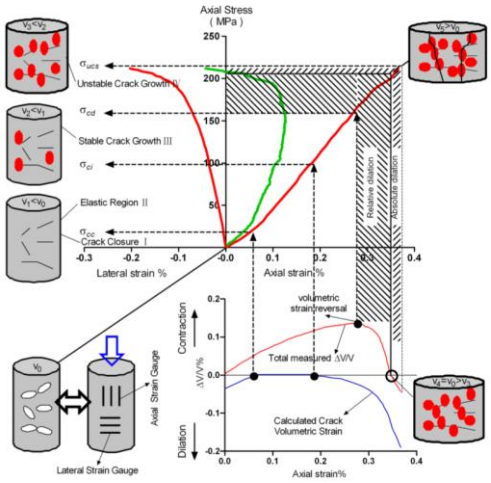

Fig. 5 Crack development phases during uniaxial compression of rock specimen (Xue *et al*. 2014)

Acoustics, PAC) were used to obtain the AE signals from the cracking event in the rock specimen. An analog filter with a range of 1–400 kHz was used in this system. The threshold was set to 40 dB, which resulted in a high signal-to-noise ratio obtained in the pre-test. For the AE hit definition, the hit lockout time (HLT), hit definition time (HDT), and peak definition time (PDT) were set to 1,000 μs, 200 μs, and 800 μs, respectively. In addition, a preamplifier (2/4/6 manufactured by PAC) was used to amplify the raw AE signal from the sensor. It is set to 40 dB gain to amplify the amplitude of the acoustic signals in this study. Sensors (Nano 30 manufactured by PAC) were used to obtain the AE signals induced by compressive loading in the specimen. The operating range and resonant frequency of the sensor were 120–750 kHz and 230 kHz, respectively.

To minimize data loss owing to the decoupling effect (e.g., detached sensor) during the loading process, six AE sensors were attached to the surface of the specimen to measure the AE hits in this study (Fig. 4). All sensors were mounted with high-vacuum grease as a coupling material tominimize attenuation between the sensor and specimen.

The sensor array was set according to previous studies on cylindrical specimens (Chang and Lee 2004, Lei *et al*. 2016, Cao *et al*. 2019). A pair of sensors were installed at the same height at the top, middle, and bottom positions of the specimen (Fig. 4). Additionally, sensors at the same height were installed opposite the position at a degree of 180 along the diameter of the specimen.

2.3 Determination of damage stage for rock specimen

Under uniaxial compressive loading conditions, the damage stages of the rock specimens with crack development patterns are described as follows: (1) elastic region, (2) plastic region with stable crack growth, and (3) plastic region with unstable crack growth (Xue *et al*. 2014). Fig. 5 shows the general crack development under uniaxial loading conditions in the stress-strain curve. Initially, elastic deformation occurred as axial stress was applied to the specimen in elastic region. This implies that the crack volumetric strain was zero (i.e., no crack generation).

Table 3 Results of stress and normalized vertical strain according to the stress ratio in specimens

Specimen	Stress ratio [%]	Stress [MPa]	Normalized vertical strain [%]
R1	50	9.3	46.4
	85	16.0	89.1
	100	18.8	100
R2	50	32.1	22.0
	85	54.8	66.8
	100	64.5	100
R3	50	11.2	12.9
	85	18.8	53.6
	100	22.1	100
R4	50	30.2	52.2
	85	51.3	82.3
	100	60.4	100
R5	50	33.3	40.7
	85	56.9	70.0
	100	66.9	100
R6	50	69.7	45.6
	85	122.1	78.1
	100	143.8	100
R7	50	50.9	49.6
	85	86.3	84.6
	100	102.0	100
R8	50	71.9	54.2
	85	122.4	84.6
	100	142.6	100

Subsequently, plastic deformation, in plastic region, occurred with new crack generation by continuous axial loading. After that, unstable plastic deformation occurred with crack expansion and connection.

The characteristics of the crack development patterns depend on the UCS of the rock specimens (Chang *et al*. 2007, Nicksiar and Martin 2012, Petružálek *et al*. 2019). The elastic deformation occurred at 50% of the UCS for the granite specimens. In addition, plastic deformation with stable crack growth occurred at 50–85% (new crack generation) and with unstable crack growth occurred at 85–100% (crack expansion and ultimate failure) of the UCS. In this study, the AE characteristics were analyzed according to three stages divided by normalized uniaxial loading from each specimen: 0–50%, 50–85%, and 85–100% UCS. Table 3 lists the stress and normalized vertical strain at 50%, 85%, and 100% stress ratios for all test specimens. The stress ratio and normalized vertical strain can be explained as Eqs. (1) and (2)

$$Stress\ ratio = \sigma/\sigma_{max} \times 100\ [\%] \quad (1)$$

$$Normalized\ vertical\ strain = \varepsilon/\varepsilon_{max} \times 100\ [\%] \quad (2)$$

where σ is the vertical stress, σ_{max} is the maximum vertical stress at ultimate failure (i.e., uniaxial compressive strength, *UCS*), ε is the vertical strain, and ε_{max} is the maximum vertical strain at ultimate failure.

2.4 Analysis Index: AE Parameter per unit Hit

The AE signal can be analyzed using time-domain parameters and frequency-domain parameters (Grosse and Ohtsu 2008). The time-domain parameters are identified as electrical signal characteristics (i.e., voltage) in the time-voltage graph, such as rise time, count, energy, and amplitude. Meanwhile, the frequency-domain parameters indicate the frequency characteristics of the acquired AE waves in the power-frequency spectrum, such as the peak frequency and frequency centroid.

Among these parameters, count, energy, and amplitude were selected to evaluate the damage stages of the rock specimens in this study. These parameters have been identified as effective for analyzing the damage characteristics of rock during compression test to induce failure of rock samples (Gu *et al*. 2019, Li *et al*. 2019, Sun *et al*. 2019). Fig. 6 illustrates the definition of the count, energy, and amplitude from the AE wave in the time-voltage graph, where the count indicates the number of points that exceed the threshold in the AE wave (blue dot in Fig. 6). Energy refers to the sum of the areas in the AE wave exceeding the threshold (red zone in Fig. 6). The

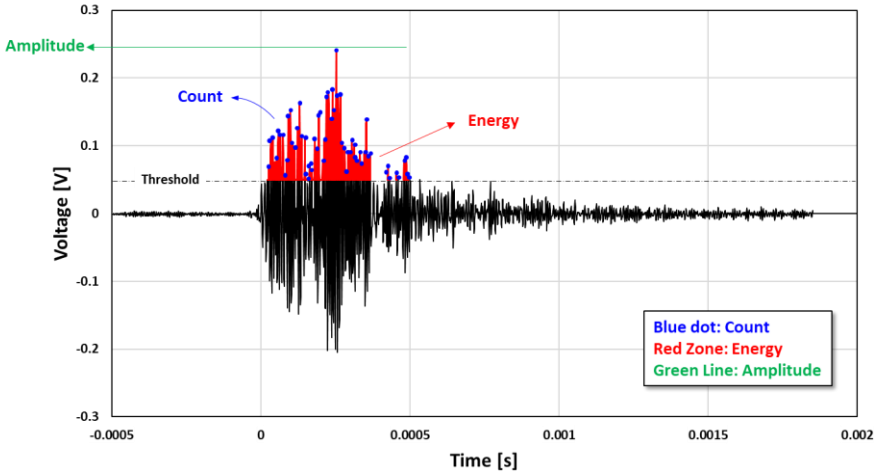

Fig. 6 Definition of AE parameters (count, energy, and amplitude) on raw signal from AE waveform

amplitude indicates the maximum voltage of the AE wave (green line in Fig. 6).

The AE parameters varied according to the loading level. In addition, the AE parameters dramatically increase when partial deformation or ultimate failure occurs by an external force, regardless of the damage stage (Tham *et al*. 2005, Vilhelm *et al*. 2008). Therefore, it is challenging to evaluate AE characteristics according to the damage stage using conventional AE parameters, such as count, energy, and amplitude. For this, the AE parameter per unit AE hit, hereafter the AE indices (i.e., count index, energy index, and amplitude index), was used as the analysis index for the characteristics of the damage stage in this study. The AE index can be expressed as Eq (3)

$$AE\ index = \left(\sum_{i=1}^{n} i\ th\ AE\ parameters\right) / n\ \ (i = 1, 2, 3, \ldots n) \quad (3)$$

where *i th AE parameters* is the parameter (i.e., count, energy, and amplitude) values of the AE hit that occurred for the i-th time.

AE signals generally occur with high strain energy and amplitude when the normalized axial stress increases (Kim *et al*. 2015). The analysis index can quantitatively represent the variation in AE parameters according to the damage stage because the analysis index denotes the value for one AE hit. This study used the AE index to evaluate the damage stage with a normalized axial stress (i.e., stress ratio) for the rock specimen. σ_{max} is the maximum vertical stress at ultimate failure.

3. Results and analysis of AE data

3.1 Characteristics of AE Hit occurrence

The AE characteristics were analyzed using cumulative AE hits according to the stress ratio. To compare the characteristics of AE hit occurrence for groups A (R1–R3) and group B (R4–R8), the cumulative AE hits were plotted with the stress ratio for all rock specimens. The stress ratio is defined as the stress value divided by the maximum stress of the vertical axis ($\sigma/\sigma_{max} \times 100$ [%]), which corresponds to the ultimate failure of each rock specimen (R1–R8). Similarly, the cumulative AE hit refers to the rate of AE hit occurrence per total AE hit measured from each specimen and sensor position (i.e., T1, T2, M1, M2, B1, and B2), as shown in Table 4. Some AE sensors were decoupled during the uniaxial loading process in specimens R1, R6, R7, and R8, and the decoupled sensor data were ignored in the analysis of the AE characteristics. In this study, the AE behavior characteristics were analyzed based on data obtained from perfectly coupled sensors on the specimens.

The cumulative AE hits increased with an increase in the stress ratio (Fig. 7) for both group A (low p-wave velocity) and group B (high p-wave velocity) specimens. In particular, the cumulative AE hit increased dramatically when the stress ratio approached 100% (near-ultimate failure). This tendency of the observed AE hit occurrence has been shown in previous research (Tham *et al*. 2005, Vilhelm *et al*. 2008). Large quantities of AE hits are generated when the stress level is close to the UCS of the specimen because of rapid macro deformation.

For specimens with high p-wave velocities (group B), AE hits were mainly generated when the stress ratio approached 100%. The cumulative AE hit was observed to occur initially at 50–60% of the stress ratio for group B specimens (R4–R8) (Fig. 7). Subsequently, the cumulative AE hit increased sharply at 80–90% of the stress ratio. In particular, the proportion of AE hits increased by 66–95%, exceeding 85% of the stress ratio. In contrast, the cumulative AE hits tended to increase gradually when the stress ratio increased for group A (R1–R3).

3.2 Characteristics of count index

The *count index* is defined as the cumulative count divided by the number of AE hits (i.e., count per unit AE hit). It is useful to analyze the variation of "count" with the

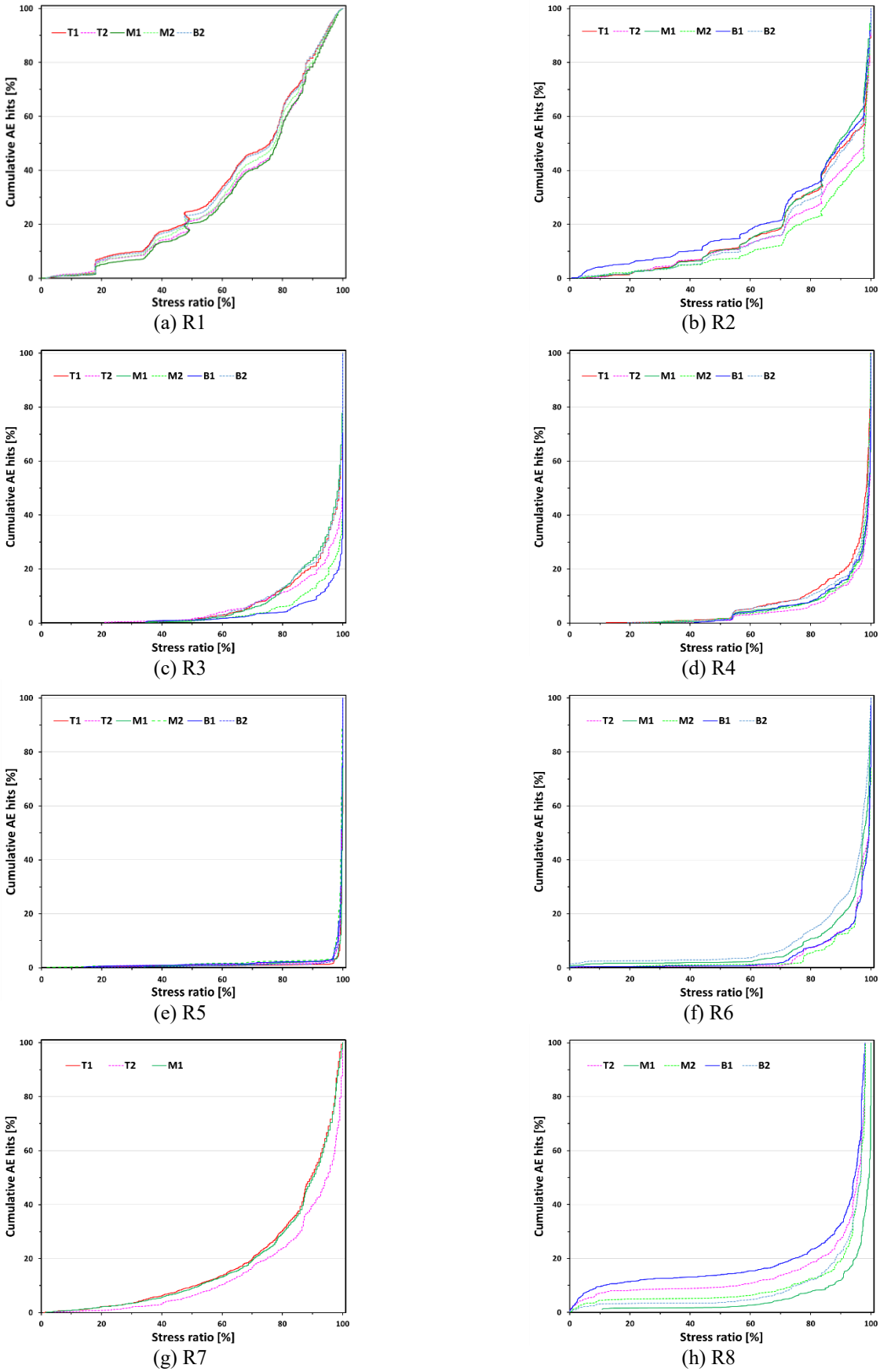

(a) R1 (b) R2

(c) R3 (d) R4

(e) R5 (f) R6

(g) R7 (h) R8

Fig. 7 Variation in cumulative AE hits with stress ratio for specimens (group A: R1–R3, group B: R4–R8)

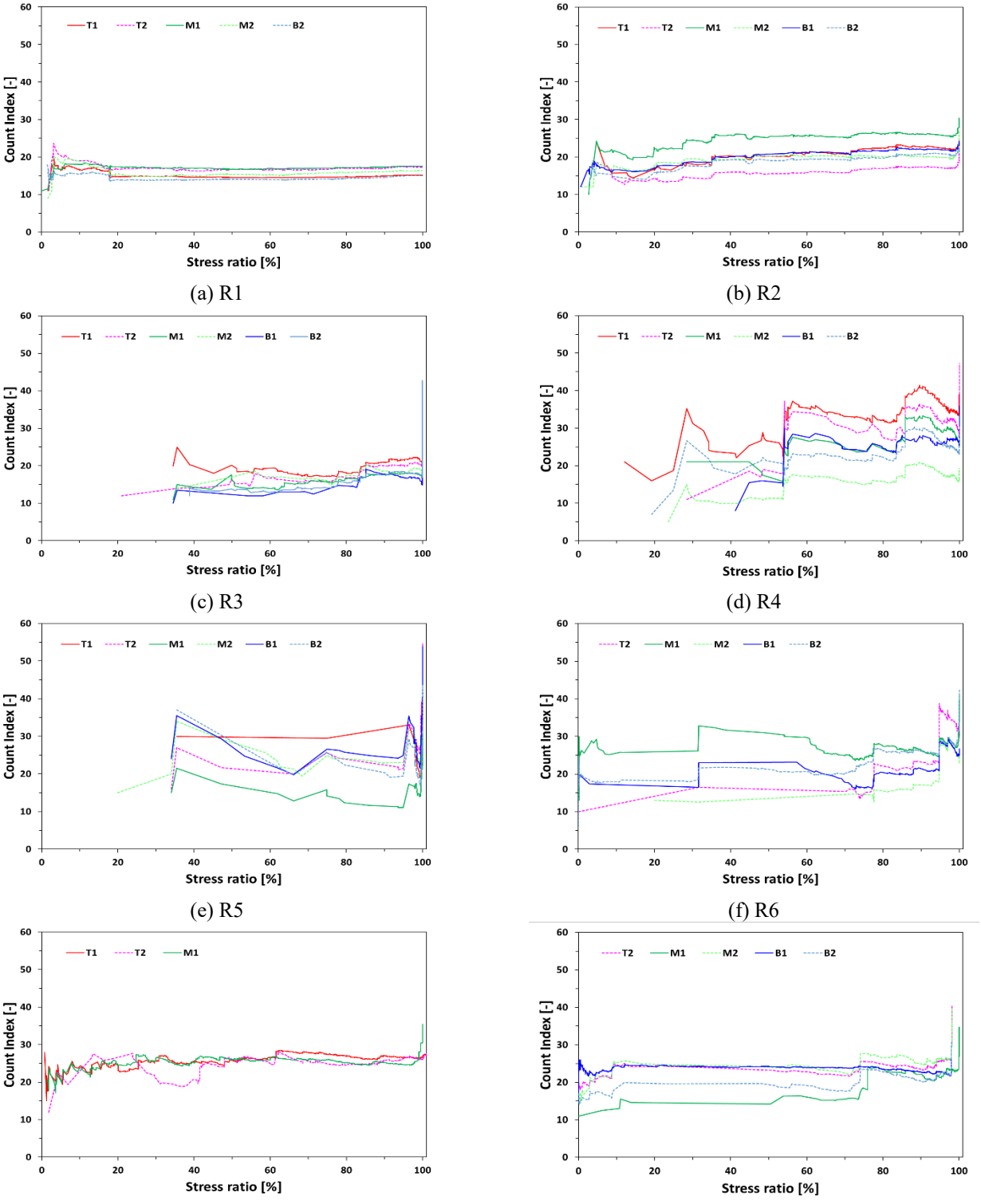

(a) R1 (b) R2

(c) R3 (d) R4

(e) R5 (f) R6

(g) R7 (h) R8

Fig. 8 Variation in count index with stress ratio for specimens (group A: R1–R3, group B: R4–R8)

increase in strain during compressive loading. Fig. 8 shows the results of the count index [-] according to the stress ratio for all specimens. The count index increased with the stress ratio. When the stress ratio approached 100% (near ultimate failure), the average count increased significantly for all specimens.

Given the results, the value of the count index was in the range of 10–25 with the stress ratio for specimens of group A (R1–R3) (Fig. 8). When the stress ratio approached 100%, the count index increased sharply and was in the range of 20–45 at ultimate failure. In contrast, the count index was in the range of 10–40 with the stress ratio for the

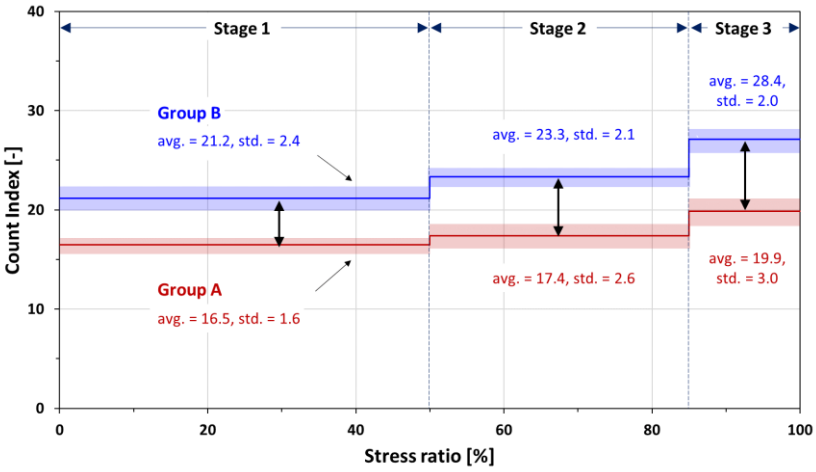

Fig. 9 Variation in count index with damage stage for group A and group B

specimens of group B (R4–R8). In addition, the count index increased suddenly in a larger range of 40–60 when the specimens were partially and ultimately deformed during compressive loading.

The count index of the group B specimens tends to vary sensitively and has a high value. Group A showed insignificant variation in the count index according to the stress ratio, except for a slight increase at ultimate failure. However, for group B, the count index tended to vary sensitively. In addition, the count index was approximately 1.9 times greater in group B than in group A; the count index was approximately 2.2 times greater in group B than in group A at ultimate failure.

Fig. 9 shows the variation in the count index for groups A and B with three damage stages based on the stress ratio; the solid line (red and blue) indicates the average count index of groups A (R1–R3) and B (R4–R8) at each stage. The shaded zone (light red and light blue) surrounding the solid line represents the standard deviation of the average count index for groups A and B at each damage stage.

The count index was found to increase as the damage stage progressed (Fig. 9). In group A, the average count index was 1.1 times greater in stage 2 than in stage 1 and 1.2 times greater in stage 3 than in stage 1. Similarly, in group B, the average count index was 1.1 times greater for stage 2 and 1.3 times greater for stage 3 than that for stage 1.

In the specimens with a high p-wave velocity (group B), the count index was greater than those with a low p-wave velocity (group A). When the damage stage progressed (stage 1 → 2 → 3), the count index increased from 16.5 → 17.4 → 19.9 for group A (Fig. 9). Meanwhile, the count index increased from 21.2 → 23.3 → 27.1 for group B. This means that the count index is sensitively changed in specimens with a high p-wave velocity.

3.3 Characteristics of energy index

The *energy index* is defined as the cumulative energy divided by the number of AE hits (i.e., energy index per unit AE hit). Fig. 10 shows the variation in the energy index [-] according to the stress ratio. The energy index increased with an increase in the stress ratio. In addition, the energy index increased dramatically at 100% of the stress ratio.

The energy index was in the range of 3–7 for the specimens of group A (R1–R3) under uniaxial compressive loading (Fig. 10). Meanwhile, the energy index of group B (R4–R8) was in the range of 3–12 with the stress ratio. In addition, the energy index increased suddenly in the range of 10–18 in the case of partial deformation and ultimate failure in the specimens of group B.

The *energy index* is defined as the cumulative energy divided by the number of AE hits (i.e., energy index per unit AE hit). Fig. 10 shows the variation in the energy index [-] according to the stress ratio. The energy index increased with an increase in the stress ratio. In addition, the energy index increased dramatically at 100% of the stress ratio.

The energy index was in the range of 3–7 for the specimens of group A (R1–R3) under uniaxial compressive loading (Fig. 10). Meanwhile, the energy index of group B (R4–R8) was in the range of 3–12 with the stress ratio. In addition, the energy index increased suddenly in the range of 10–18 in the case of partial deformation and ultimate failure in the specimens of group B.

3.4 Characteristics of amplitude index

The AE signals can be analyzed using the amplitude, which is defined as the maximum voltage in the gathered AE waveforms. A threshold level of 40 dB was determined to maximize the acquisition of cracking signals from rock specimens while minimizing the acquisition of noise signals in the AE system (Wu *et al*. 2000, Chen *et al*. 2005, Oh *et al*. 2020). In the test system, 100 dB is the maximum amplitude that can be detected for the AE signals generated by the cracking of rock specimens. Thus, the amplitude range is 40–100 dB.

Fig. 12 shows the variation in the *amplitude index* (i.e., amplitude per unit AE hit) according to the stress ratio under uniaxial compressive loading. Regardless of the material properties of the specimens, the amplitude index was measured in the range of 45–60 dB. For the specimens

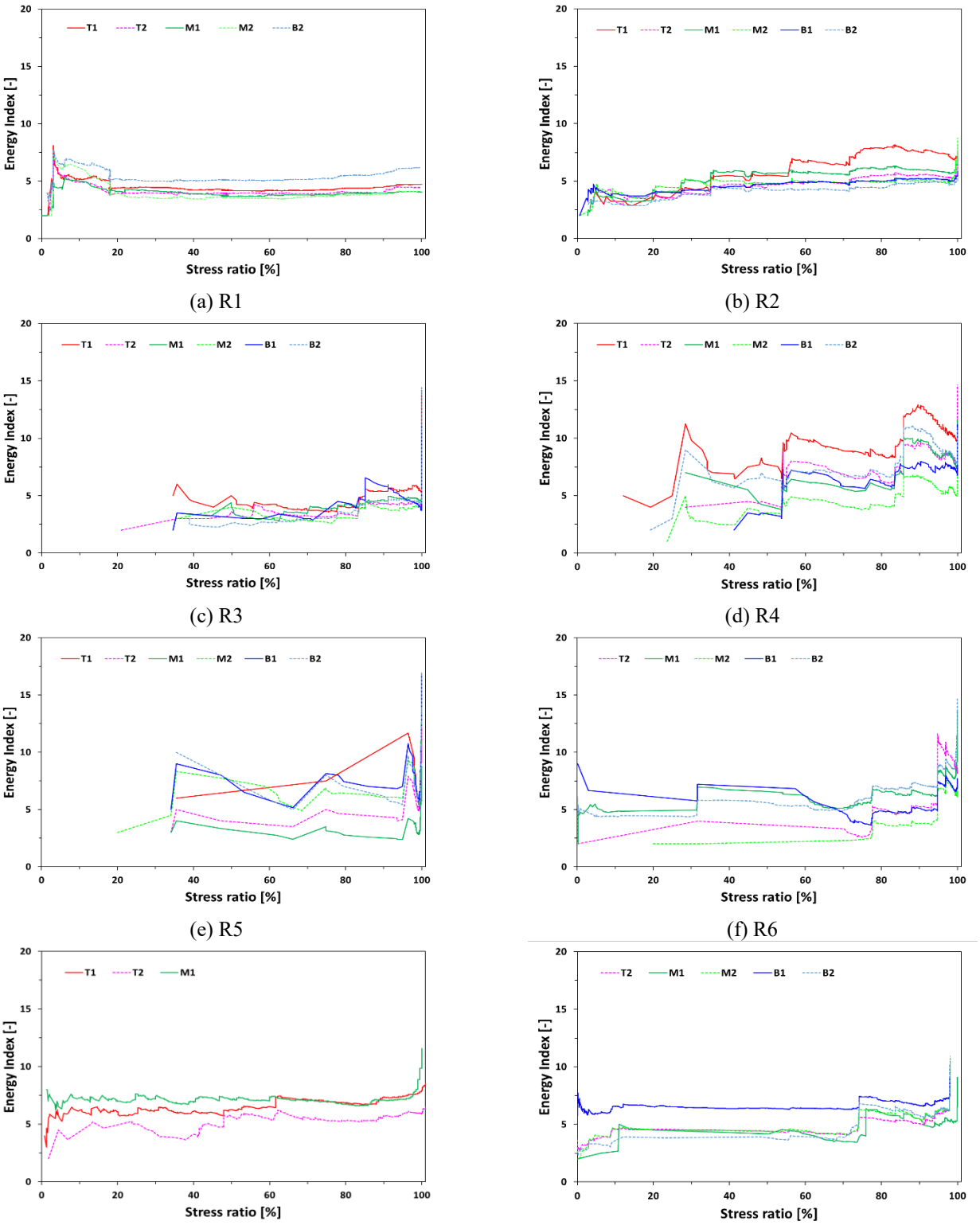

(a) R1 (b) R2

(c) R3 (d) R4

(e) R5 (f) R6

(g) R7 (h) R8

Fig. 10 Variation in energy index with stress ratio for specimens (group A: R1–R3, group B: R4–R8)

of group A (R1–R3), the amplitude index was almost constant at 55–58 dB when the stress ratio was increased. In contrast, the amplitude index increased slightly with an increase in the stress ratio for group B (R1–R3); the amplitude indices were obtained as 50–56 dB (R4), 51–53 dB (R5), 52–55 dB (R6), 48–55 dB (R7), and 52–55 dB (R8) when the stress ratio increased (0% → 100%).

On comparing the count and energy indices, the amplitude index is considered an unsuitable analysis index for evaluating the cracking of rock specimens. This is

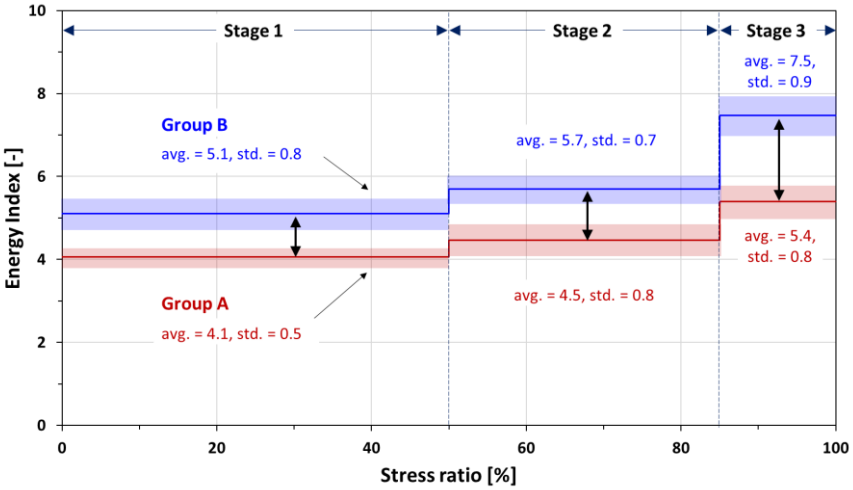

Fig. 11 Variation in energy index with damage stage for group A and group B

because the amplitude has a low sensitivity from 40–100 dB rather than the other analysis indices (e.g., count and energy). In addition, the variation in the amplitude index with the stress ratio was too small (within 10 dB). Therefore, the amplitude index is used as an inappropriate analysis index to evaluate the cracking and ultimate failure of rock specimens.

The tendency of the amplitude index was observed to be opposite to that of the count index and energy index; the averaged amplitude index was found to be low for specimens with high p-wave velocity (Fig. 13). The amplitude index increased as 52.7 (stage 1) → 54.5 (stage 2) → 56.4 (stage 3) according to the damage stage in the case for group B. In addition, it is clearly shown that the amplitude index increases according to the progressive damage stage. Meanwhile, the amplitude index varies as 56.3 (stage 1) → 56.4 (stage 2) → 56.0 (stage 3) according to the damage stage in the case of group A. The value shows little change according to the damage stage and converges to 56.0 dB.

4. Discussion

4.1 Rock properties effects

The AE characteristics were affected by the material properties of the rock under compressive loading conditions. Given the test results, the count index and energy index have greater values in specimens with high p-wave velocities (Figs. 9 and 11). To investigate the AE characteristics according to the material properties of the rock, the dynamic (e.g., p-wave velocity) and static (e.g., density, UCS, and Young's modulus) properties, which are related to wave propagation, were considered in this study. The detailed properties of the specimens are presented in Table 2.

The AE indices (i.e., count, energy, and amplitude) are plotted according to the values of the material properties of the rock at damage stage 1 (Fig. 14), stage 2 (Fig. 15), and stage 3 (Fig. 16). The values of the material property correspond in a range of 2,416.7–5,833.3 m/s (p-wave velocity), 2.62–3.06 g/cm3 (density), 18.8–143.8 MPa (UCS), and 3.02–66.23 GPa (Young's modulus), respectively. To investigate the effect of rock properties on the AE characteristics, the variation rate of the AE index was analyzed according to the rock properties at three damage stages.

In damage stage 1 (stress ratio in the range of 0–50%), the count index and energy index increased by 33.2% and 25.6%, respectively, with an increase in the p-wave velocity (Fig. 14(a)). Meanwhile, the amplitude index decreased by 7.8% with an increase in p-wave velocity. Likewise, the AE index tended to have similar patterns in density, UCS, and Young's modulus. The count index and energy index increased by 22.5% and 10.6%, respectively, and the amplitude index decreased by 7.6% with an increase in density (Fig. 14(b)). In addition, the count index and energy index increased by 18.6% and 9.2%, respectively, and the amplitude index decreased by 7.2% with an increase in UCS (Fig. 14(c)). When the Young's modulus increased, the count index and energy index increased by 53.8% and 43.3%, respectively, and the amplitude index decreased by 5.8% (Fig. 14(d)).

These tendencies are similar in damage stage 2 (stress ratio in the 50–85% range) and stage 3 (stress ratio in the 85–100% range). In damage stage 2, the count index and energy index increased by 39.1% and 31.1%, respectively, with an increase in the p-wave velocity (Fig. 15(a)). Meanwhile, the amplitude index decreased by 5.4% with an increase in p-wave velocity. The count index and energy index increased by 20.9% and 7.5%, respectively, and the amplitude index decreased by 5.1% with an increase in density (Fig. 15(b)). In addition, the count index and energy index increased by 26.6% and 18.7%, respectively, and the amplitude index decreased by 5.1% with an increase in the UCS (Fig. 15(c)). Finally, the count index and energy index increased by 41.4% and 37.8%, respectively, and the amplitude index decreased by 4.2% with an increase in the Young's modulus (Fig. 15(d)).

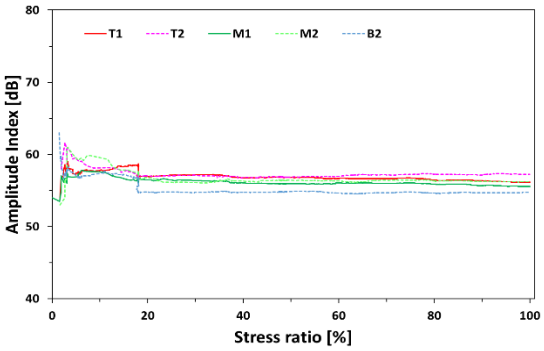

(a) R1

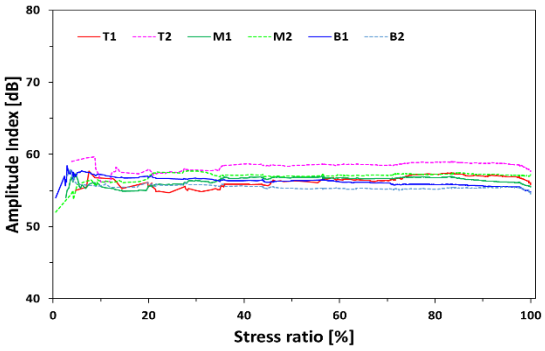

(b) R2

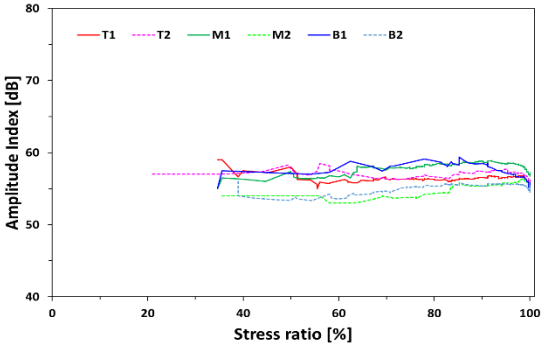

(c) R3

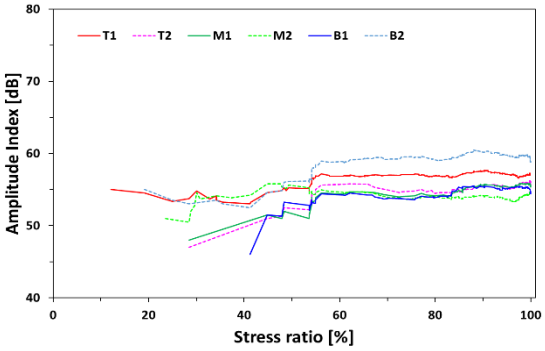

(d) R4

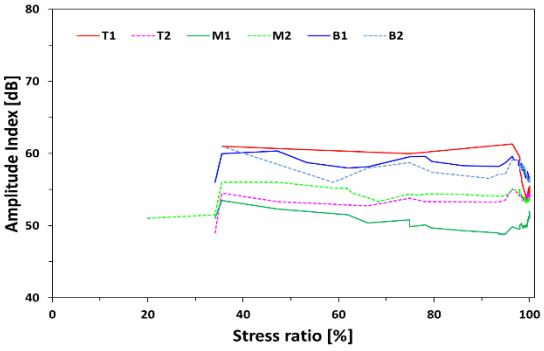

(e) R5

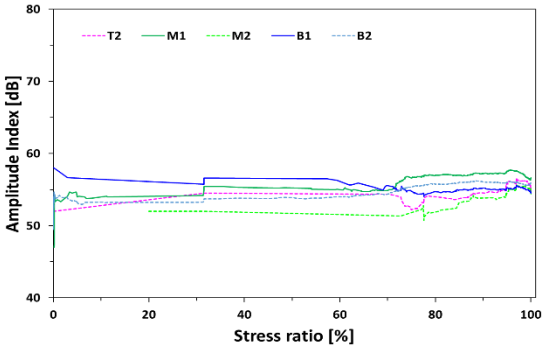

(f) R6

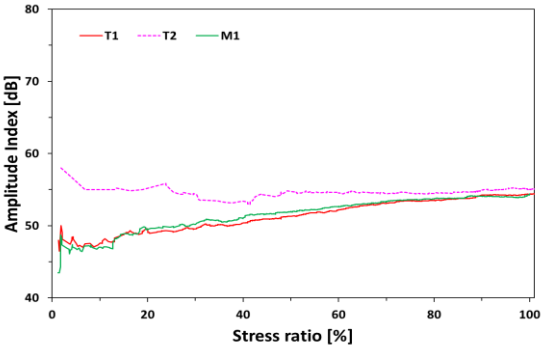

(g) R7

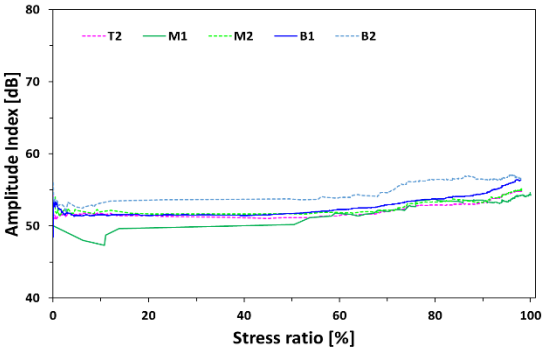

(h) R8

Fig. 12 Variation in amplitude index with stress ratio for specimens (group A: R1–R3, group B R4–R8)

In damage stage 3, the count index and energy index increased by 42.0% and 42.7%, respectively with an increase of p-wave velocity, whereas the amplitude index decreased by 2.4% when the p-wave velocity increased (Fig. 16(a)). The count index and energy index increased by 30.3% and 26.0%, respectively, and the amplitude index decreased by 2.5% with an increase in density (Fig. 16(b)). In addition, the count index and energy index increased by 29.3% and 25.1%, respectively, and the amplitude index decreased by 1.3% with an increase in UCS (Fig. 16(c)).

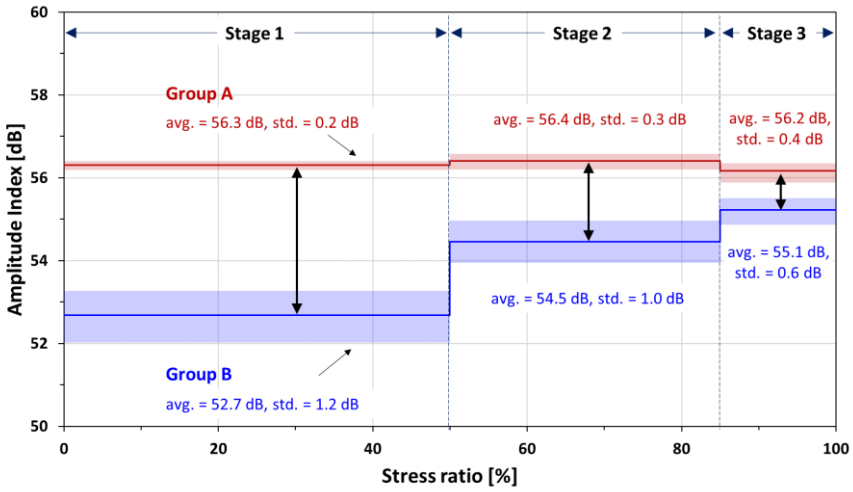

Fig. 13 Variation in amplitude index with damage stage for group A and group B

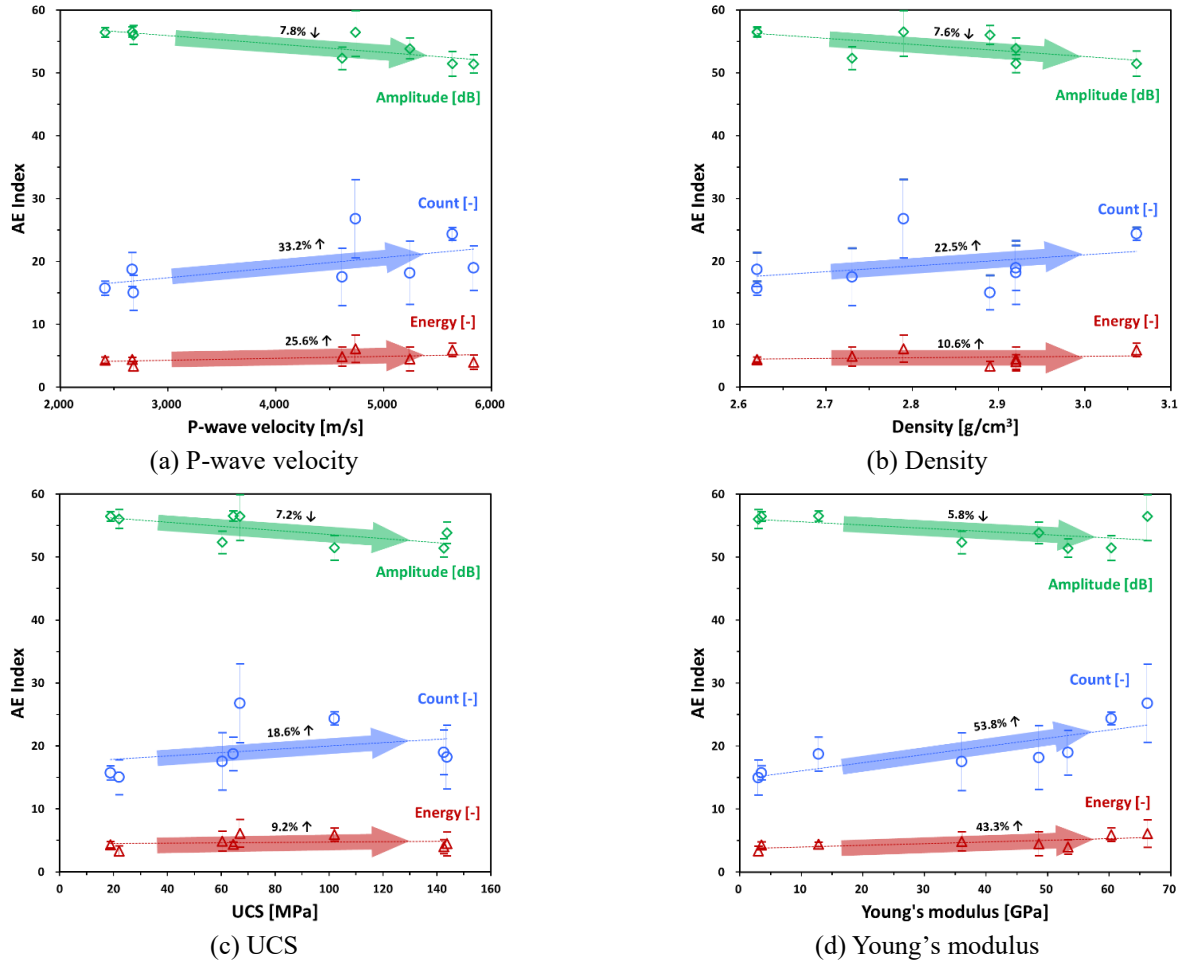

(a) P-wave velocity (b) Density

(c) UCS (d) Young's modulus

Fig. 14 AE index variation according to material properties at damage stage 1 (stress ratio: 0–50%) for granite specimens

The count index and energy index increased by 50.2% and 53.9%, respectively, and the amplitude index decreased by 5.7%, increasing the Young's modulus (Fig. 16(d)).

Given the above results, it is evident that the count index and energy index increase with higher values of material properties, while the amplitude index shows a decreasing trend under similar conditions. These trends are particularly pronounced in damage stage 3, indicating a greater sensitivity of AE indices to variations in material properties as the damage stages progress. This pattern highlights a clear relationship between AE parameters and the scale of cracks, which is closely linked to the internal

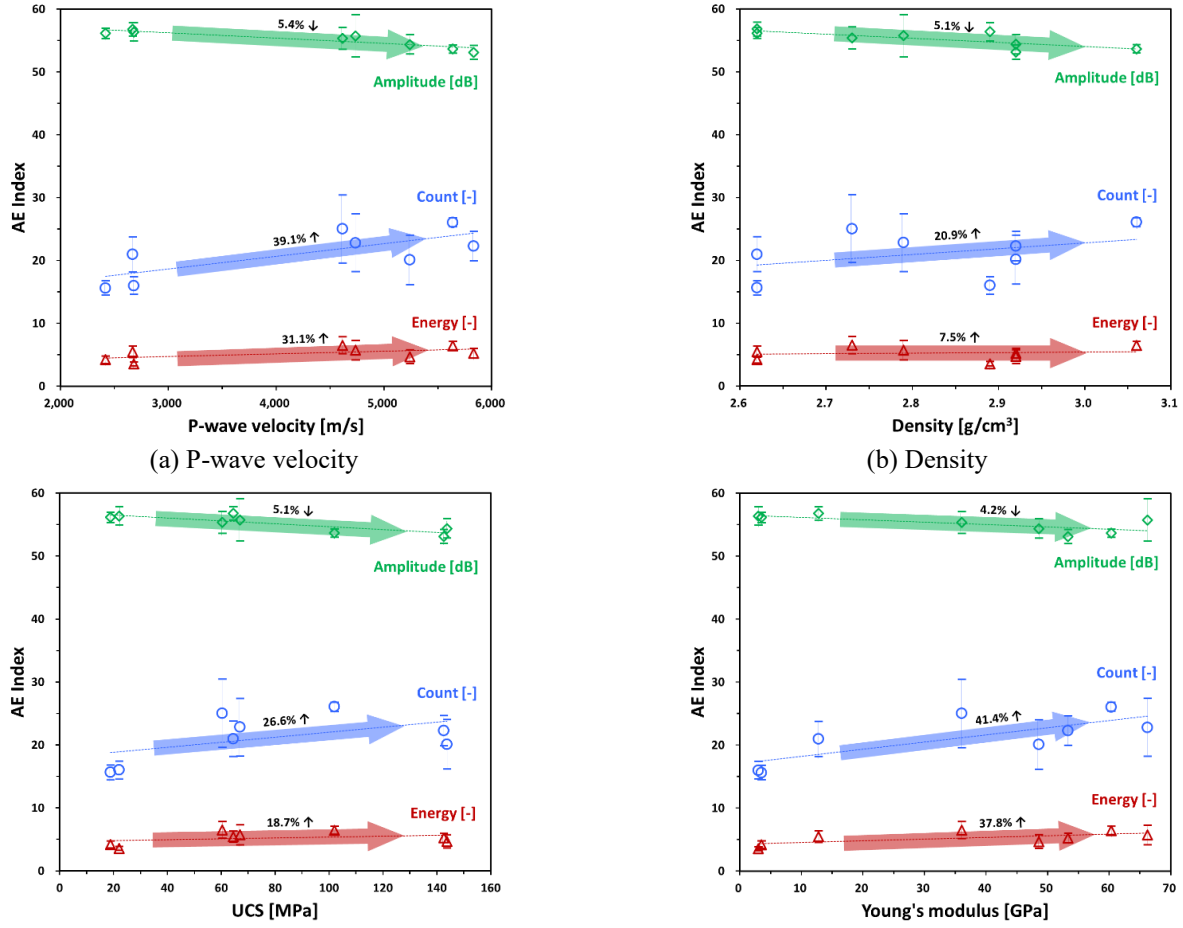

(a) P-wave velocity (b) Density

(c) UCS (d) Young's modulus

Fig. 15 AE index variation according to material properties at damage stage 2 (stress ratio: 50–85%) for granite specimens

structure and heterogeneity of rock samples.

The variation of AE parameters (counts, energy, amplitude) is directly related to the scale of cracks within the rock samples. This relationship highlights the importance of considering the internal structure and heterogeneity of rock samples when analyzing AE characteristics. Moreover, discussions on macroscopic failure predictability and its relationship with AE parameters, such as rock samples with different p-wave velocity, density, UCS, and Young's modulus, would provide valuable insights. As demonstrated in Fig. 7, which illustrates first-order and second-order phase transitions with cumulative AE hits for different rock samples, such predictability is evident. These phase transitions are influenced by the heterogeneity of the rock samples and play a crucial role in understanding macroscopic failure behavior (Cartwright-Taylor *et al*. 2020, Mo *et al*. 2023). Therefore, further exploration of these relationships would enhance our understanding of AE characteristics in rock mechanics and improve the predictability of macroscopic failure based on AE parameters and material properties.

4.2 Determination of optimal AE index with rock property

When the material properties are considered to recognize cracking in the rock medium using AE parameters, the most appropriate analysis index is determined as the count index. The variation in the amplitude index was insignificant according to the rock properties (Figs. 14-16). Furthermore, the sensitivity of the amplitude was lower than that of the count and energy. Although the energy index showed a significant increase rate with variation in rock properties in all damage stages, the change in absolute values was too small (values were approximately 3–8). The energy index has limitations in the application of rock stability monitoring. Therefore, the count index, which has a high sensitivity for recognizing cracking in rock specimens, was evaluated as an effective analysis index to monitor rock damage using the AE technique.

Among the material properties of rock specimens, Young's modulus and p-wave velocity were estimated to be sensitive properties for the count index. In damage stage 1 (Fig. 14), the increase rate of the count index is greater for Young's modulus of approximately 30% than that for the density and UCS; the increase rate of the count index is greater for a p-wave velocity of approximately 10% than that for the density and UCS. In damage stage 2 (Fig. 15) and 3 (Fig. 16), similarly, the increase rate of count index is

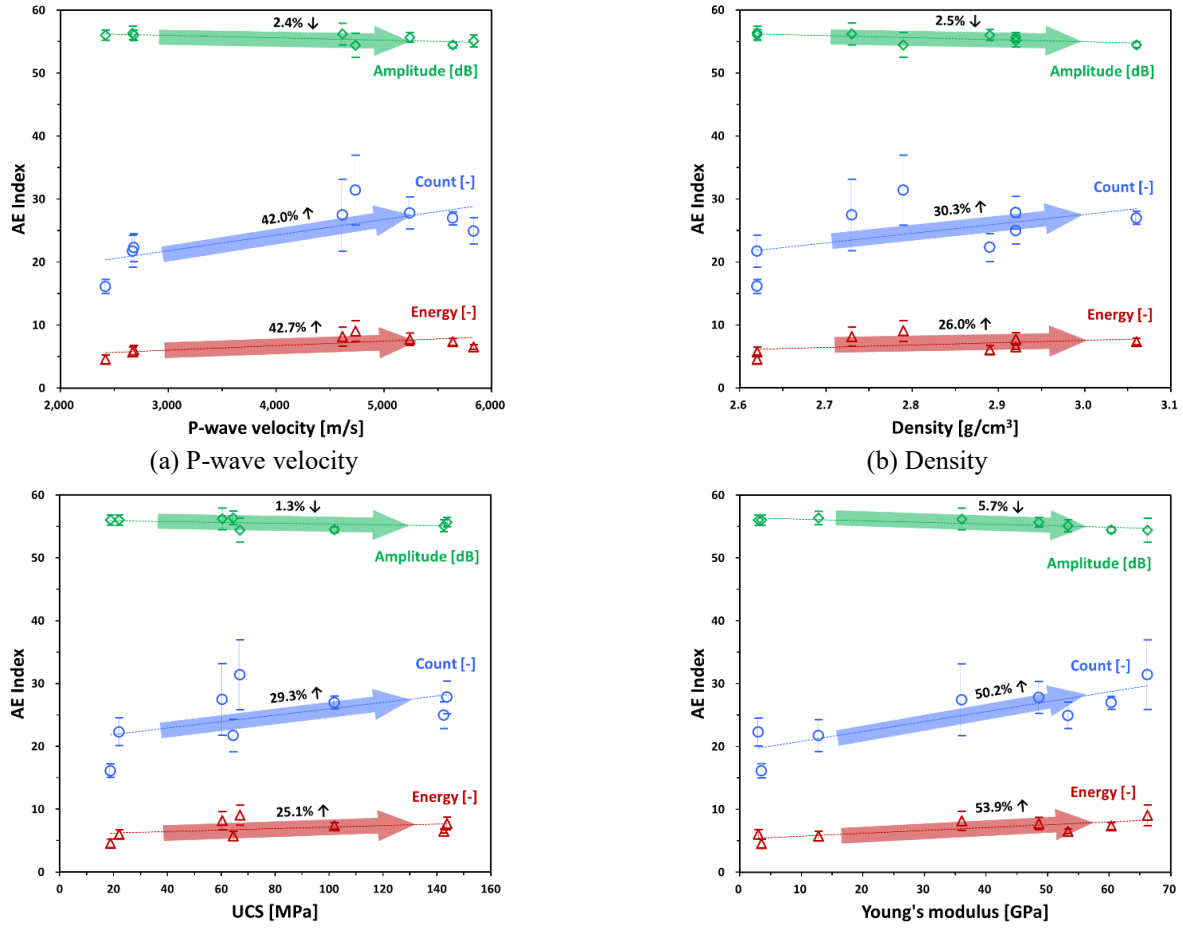

(a) P-wave velocity (b) Density

(c) UCS (d) Young's modulus

Fig. 16 AE index variation according to material properties at damage stage 3 (stress ratio: 85–100%) for granite specimens

Table 4 Correlation matrix for AE indices and rock properties at damage stage 1

	CI	*EI*	*AI*	V_p	ρ	*UCS*	*E*
CI	1.000						
EI	0.841	1.000					
AI	-0.643	-0.534	1.000				
V_p	0.669	0.465	-0.927	1.000			
ρ	0.364	0.107	-0.681	0.717	1.000		
UCS	0.362	0.127	-0.689	0.847	0.592	1.000	
E	0.828	0.558	-0.782	0.924	0.594	0.721	1.000

Table 5 Correlation matrix for AE indices and rock properties at damage stage 2

	CI	*EI*	*AI*	V_p	ρ	*UCS*	*E*
CI	1.000						
EI	0.940	1.000					
AI	-0.524	-0.327	1.000				
V_p	0.757	0.558	-0.896	1.000			
ρ	0.391	0.104	-0.745	0.717	1.000		
UCS	0.523	0.313	-0.827	0.847	0.592	1.000	
E	0.780	0.625	-0.716	0.924	0.594	0.721	1.000

CI: Count Index, *EI*: Energy Index, *AI*: Amplitude Index

greater for Young's modulus by approximately 20% than the density and UCS; the increase rate of count index is greater for p-wave velocity by approximately 15% than the density and UCS.

These trends can be identified through correlation matrix analysis. Tables 4 to 6 present the Pearson's correlation coefficients corresponding to each damage stage. Correlation matrix analysis was performed in accordance with the statistical process outlined by Triyaki (2008). Pearson's correlation coefficient, ranging from -1 to 1, indicates negative correlation as values approach -1, and positive correlation as values approach 1. From the analysis, the count index exhibits stronger correlations with rock properties compared to the energy index and amplitude index. Furthermore, significant Pearson's correlation coefficients were observed with p-wave velocity and Young's modulus, with these relationships becoming more discernible as the damage stage progressed (1→3).

Therefore, considering the material properties of rock is important to detect cracking in a rock medium using an AE monitoring technique. In a rock medium, the p-wave velocity depends on porosity because the AE wave propagates through the particles in the rock (Zhukov and

Table 6 Correlation matrix for AE indices and rock properties at damage stage 3

	CI	*EI*	*AI*	V_p	ρ	*UCS*	*E*
CI	1.000						
EI	0.972	1.000					
AI	-0.769	-0.702	1.000				
V_p	0.848	0.780	-0.771	1.000			
ρ	0.512	0.360	-0.515	0.717	1.000		
UCS	0.636	0.567	-0.562	0.847	0.592	1.000	
E	0.954	0.901	-0.905	0.924	0.594	0.721	1.000

Kuzmin 2020). In addition, the particle arrangement is disturbed when an external force is continuously applied tothe medium. Consequently, the porosity increases, and the dynamic characteristics (e.g., p-wave velocity) change due to rock crack generation (Yang *et al*. 2017). In addition, the static characteristics (e.g., density, UCS, and Young's modulus) are strongly related to the p-wave velocity, which increases with UCS and Young's modulus (Chawre 2018).

5. Conclusions

The AE technique has been used to estimate rock deformations in underground environments with limited accessibility. To explore the AE characteristics according to the rock properties and damages, a uniaxial compressive test was conducted using an AE measurement system to analyze the AE characteristics (i.e., count index, energy index, and amplitude index) with three damage stages. The concluding remarks are as follows.

- The count index and energy index were evaluated to be approximately 30% greater for specimens with high velocity (group A) than for those with low velocity (group B) at all damage stages. Meanwhile, the amplitude index tended to be greater in group B than in group A. In addition, the AE indices (i.e., count index, energy index, and amplitude index) increased with the progress in the damage stages under uniaxial loading conditions.
- When the damage stage progressed (damage stage 1 → 3), the count index and energy index increased by 21–28% and 32-47%, respectively. Meanwhile, the amplitude index converged to 56 dB as the damage stages progressed.
- The material properties affecting the AE characteristics were determined using the p-wave velocity, density, UCS, and Young's modulus. The AE index was sensitive to changes in the p-wave velocity and Young's modulus at all damage stages.
- The most appropriate analysis index is the count index, which has high sensitivity according to the rock properties and damage stages. Meanwhile, the energy index and amplitude index were evaluated as less sensitive indices because the variation in absolute values was too small.

Acknowledgments

This research was supported by the National Research Foundation of Korea (NRF) grant funded by the Korea Government (MSIT) (No. NRF-2022R1I1A3065299) and by the Brain Korea 21 FOUR Project in the Education & Research Center for Infrastructure of Smart Ocean City (i-SOC Center) (Grant No. 4199990614525).

References

Aker, E., Kühn, D., Vavryčuk, V., Soldal, M. and Oye, V. (2014), "Experimental investigation of acoustic emissions and their moment tensors in rock during failure", *Int. J. Rock. Mech. Min. Sci.*, **70**, 286-295. https://doi.org/10.1016/j.ijrmms.2014.05.003.

ASTM D2938 (2002), Standard test method for unconfined compressive strength of intact rock core specimens, ASTM International, West Conshohocken, PA, USA.

Bieniawski, Z.T. and Bernede, M.J. (1979), "Suggested methods for determining the uniaxial compressive strength and deformability of rock materials: Part 1. Suggested method for determining deformability of rock materials in uniaxial compression", *Int. J. Rock Mech. Min. Sci. Geomech. Abstr*. **16**(2), 138-140. https://doi.org/10.1016/0148-9062(79)91451-7.

Brown, E.T. (1981), ISRM suggested methods. Rock characterization testing and monitoring, Pergamon Press, Oxford, UK.

Cao, A., Jing, G., Ding, Y.L. and Liu, S. (2019), "Mining-induced static and dynamic loading rate effect on rock damage and acoustic emission characteristic under uniaxial compression", *Saf. Sci*., **116**, 86-96. https://doi.org/10.1016/j.ssci.2019.03.003.

Cartwright-Taylor, A., Main, I.G., Butler, I.B., Fusseis, F., Flynn, M. and King, A. (2020), "Catastrophic failure: how and when? Insights from 4-D in situ x-ray microtomography", *J. Geophys. Res. Solid Earth*, **125**(8), e2020JB019642. https://doi.org/10.1029/2020JB019642.

Chang, S.H., Lee, C.I. and Lee, Y.K. (2007), "An experimental damage model and its application to the evaluation of the excavation damage zone", *Rock Mech. Rock Eng*., **40**(3), 245-285. https://doi.org/10.1007/s00603-006-0113-8.

Chang, S.H. and Lee, C.I. (2004), "Estimation of cracking and damage mechanisms in rock under triaxial compression by moment tensor analysis of acoustic emission", *Int. J. Rock Mech. Min. Sci*., **41**(7), 1069-1086. https://doi.org/10.1016/j.ijrmms.2004.04.006.

Chawre, B. (2018), "Correlations between ultrasonic pulse wave velocities and rock properties of quartz-mica schist", *J. Rock Mech. Geotech. Eng*., **10**(3), 594-602. https://doi.org/10.1016/j.jrmge.2018.01.006.

Chen, B., Liu, J. and Wu, K. (2005), "Electrical responses of carbon fiber reinforced cementitious composites to monotonic and cyclic loading", *Cem. Concr. Res*., **35**(11), 2183-2191. https://doi.org/10.1016/j.cemconres.2005.02.004.

Costin, L.S. (1997), Site selection and characterization processes for deep geologic disposal of high level nuclear waste, Sandia National Laboratories, Alberquerque, NM, USA.

Fairhurst, C. (2004), "Nuclear waste disposal and rock mechanics: contributions of the Underground Research Laboratory (URL), Pinawa, Manitoba, Canada", *Int. J. Rock Mech. Min. Sci*., **41**(8), 1221-1227. https://doi.org/10.1016/j.ijrmms.2004.09.001.

Fu, B. and Tang, C.A. (2021), "Acoustic emission characteristics of marble under uniaxial cyclic loading", *Geomech. Eng.*, **27**(4), 347-359. https://doi.org/10.12989/gae.2021.27.4.347.

Gong, Y., Song, Z., He, M., Gong, W. and Ren, F. (2017), "Precursory waves and eigenfrequencies identified from

acoustic emission data based on singular spectrum analysis and laboratory rock-burst experiments", *Int. J. Rock Mech. Min. Sci.*, **91**, 155-169. https://doi.org/10.1016/j.ijrmms.2016.11.020.

Granger, S., Loukili, A., Pijaudier-Cabot, G. and Chanvillard, G. (2007), "Experimental characterization of the self-healing of cracks in an ultra high performance cementitious material: Mechanical tests and acoustic emission analysis", *Cement Concrete Res.*, **37**(4), 519-527. https://doi.org/10.1016/j.cemconres.2006.12.005.

Grosse, C.U. and Ohtsu, M. (2008), Acoustic emission testing, Springer, Heidelberg, Germany.

Gu, Q., Ma, Q., Tan, Y., Jia, Z., Zhao, Z. and Huang, D. (2019), "Acoustic emission characteristics and damage model of cement mortar under uniaxial compression", *Constr. Build. Mater.*, **213**, 377-385. https://doi.org/10.1016/j.conbuildmat.2019.04.090.

Howard, A.J. (1991), "Request for information ITA study of non-destructive methods of inspecting and testing tunnel linings", *Tunn. Undergr. Space Tech.*, **6**(4), 469. https://doi.org/10.1016/0886-7798(91)90103-B.

Hudson, J.A., Cosgrove, J.W., Kemppainen, K. and Johansson, E. (2011), "Faults in crystalline rock and the estimation of their mechanical properties at the Olkiluoto site, western Finland", *Eng. Geol.*, **117**(3-4), 246–258. https://doi.org/10.1016/j.enggeo.2010.11.004.

Ishida, T., Labuz, J.F., Manthei, G., Meredith, P.G., Nasseri, M.H.B., Shin, K., Yokoyama, T. and Zang, A. (2017), "ISRM suggested method for laboratory acoustic emission monitoring", *Rock Mech. Rock Eng.*, **50**(3), 665-674. https://doi.org/10.1007/s00603-016-1165-z.

Kim, J.S., Lee, K.S., Cho, W.J., Choi, H.J. and Cho, G.C. (2015), "A comparative evaluation of stress–strain and acoustic emission methods for quantitative damage assessments of brittle rock", *Rock Mech. Rock Eng.*, **48**(2), 495-508. https://doi.org/10.1007/s00603-014-0590-0.

Kim, M.J., Lee, S.R., Yoon, S., Jeon, J.S. and Kim, M.S. (2018), "Optimal initial condition of a bentonite buffer with regard to thermal behavior in a high-level radioactive waste repository", *Comput. Geotech.*, **104**, 109-117. https://doi.org/10.1016/j.compgeo.2018.08.011.

Lee, J.W., Kim, H. and Oh, T.M. (2020), "Acoustic emission characteristics during uniaxial compressive loading for concrete specimens according to sand content ratio", *KSCE J. Civ. Eng.*, **24**(9), 2808-2823. https://doi.org/10.1007/s12205-020-5697-0.

Lei, X., Funatsu, T., Ma, S. and Liu, L. (2016), "A laboratory acoustic emission experiment and numerical simulation of rock fracture driven by a high-pressure fluid source", *J. Rock Mech. Geotech. Eng.*, **8**(1), 27-34. https://doi.org/10.1016/j.jrmge.2015.02.010.

Li, H., Shen, R., Li, D., Jia, H., Li, T., Chen, T. and Hou, Z. (2019), "Acoustic emission multi-parameter analysis of dry and saturated sandstone with cracks under uniaxial compression", *Energies*, **12**(10), 1959. https://doi.org/10.3390/en12101959.

Li, C.J., Lou, P.J. and Xu, Y. (2022), "Damage characterization of hard-brittle rocks under cyclic loading based on energy dissipation and acoustic emission characteristics", *Geomech. Eng.*, **31**(4), 365-373. https://doi.org/10.12989/gae.2022.31.4.365.

Meng, F., Wong, L.N.Y., Zhou, H., Yu, J. and Cheng, G. (2019), "Shear rate effects on the post-peak shear behaviour and acoustic emission characteristics of artificially split granite joints", *Rock Mech. Rock Eng.*, **52**(7), 2155-2174. https://doi.org/10.1007/s00603-018-1722-8.

Mo, C., Zhao, J. and Zhang, D. (2023), "Mode I microscopic cracking process of granite considering the criticality of failure", *J. Geophys. Res. Solid Earth*, **128**(10), e2023JB027040. https://doi.org/10.1029/2023JB027040.

Nejati, H.R. and Ghazvinian, A. (2014), "Brittleness effect on rock fatigue damage evolution", *Rock Mech. Rock Eng.*, **47**(5), 1839-1848. https://doi.org/10.1007/s00603-013-0486-4.

Nicksiar, M. and Martin, C.D. (2012), "Evaluation of methods for determining crack initiation in compression tests on low-porosity rocks", *Rock Mech. Rock Eng.*, **45**(4), 607-617. https://doi.org/10.1007/s00603-012-0221-6.

Niu, Y., Wang, J., Hu, Y., Wang, G. and Liu, B. (2023), "Time-frequency domain characteristics of intact and cracked red sandstone based on acoustic emission waveforms", *Geomech. Eng.*, **34**(1), 1-15. https://doi.org/10.12989/gae.2023.34.1.001.

Oh, T.M., Kim, M.K., Lee, J.W., Kim, H. and Kim, M.J. (2020), "Experimental investigation on effective distances of acoustic emission in concrete structures", *Appl. Sci.*, **10**(17), 6051. https://doi.org/10.3390/app10176051.

Petružálek, M., Lokajíček, T., Svitek, T., Jechumtálová, Z., Kolář, P. and Šílený, J. (2019), "Fracturing of migmatite monitored by acoustic emission and ultrasonic sounding", *Rock Mech. Rock Eng.*, **52**, 47-59. https://doi.org/10.3390/app10176051.

Siren, T., Hakala, M., Valli, J., Kantia, P., Hudson, J.A. and Johansson, E. (2015), "In situ strength and failure mechanisms of migmatitic gneiss and pegmatitic granite at the nuclear waste disposal site in Olkiluoto, Western Finland", *Int. J. Rock Mech. Min. Sci.*, **79**, 135-148. https://doi.org/10.1016/j.ijrmms.2015.08.012.

Sun, B., Hou, S., Xie, J. and Zeng, S. (2019), "Failure prediction of two types of rocks based on acoustic emission characteristics", *Adv. Civ. Eng.*, 2019, 5028489. https://doi.org/10.1155/2019/5028489.

Stoeckher, F., Molenda, M., Brenne, S. and Alber, M. (2015), "Fracture propagation in sandstone and slate–Laboratory experiments, acoustic emissions and fracture mechanics", *J. Rock Mech. Geotech. Eng.*, **7**(3), 237-249. https://doi.org/10.1016/j.jrmge.2015.03.011.

Tham, L.G., Liu, H., Tang, C.A., Lee, P.K.K. and Tsui, Y. (2005), "On tension failure of 2-D rock specimens and associated acoustic emission", *Rock Mech. Rock Eng.*, **38**(1), 1-19. https://doi.org/10.1007/s00603-004-0031-6.

Tiryaki, B. (2008), "Predicting intact rock strength for mechanical excavation using multivariate statistics, artificial neural networks, and regression trees", *Eng. Geol.*, **99**(1-2), 51-60. https://doi.org/10.1016/j.enggeo.2008.02.003.

Vilhelm, J., Rudajev, V., Lokajíček, T. and Veverka, J. (2008), "Correlation analysis of the ultrasonic emission from loaded rock samples–the study of interaction of microcracking nucleation centres", *Rock Mech. Rock Eng.*, **41**(5), 695-714. https://doi.org/10.1007/s00603-006-0114-7.

Wang, J., Chen, L., Su, R. and Zhao, X. (2018), "The Beishan underground research laboratory for geological disposal of high-level radioactive waste in China: planning, site selection, site characterization and in situ tests", *J. Rock Mech. Geotech. Eng.*, **10**(3), 411-435. https://doi.org/10.1016/j.jrmge.2018.03.002.

Wang, Q., Chen, J., Guo, J., Luo, Y., Wang, H. and Liu, Q. (2019), "Acoustic emission characteristics and energy mechanism in karst limestone failure under uniaxial and triaxial compression", *Bull. Eng. Geol. Environ.*, **78**(3), 1427-1442. https://doi.org/10.1007/s10064-017-1189-y.

Wang, Z., Wang, J., Yang, S., Li, L. and Li, M. (2020), "Failure behaviour and acoustic emission characteristics of different rocks under uniaxial compression", *J. Geophys. Eng.*, **17**(1), 76-88. https://doi.org/10.1093/jge/gxz092.

Wu, K., Chen, B. and Yao, W. (2000), "Study on the AE characteristics of fracture process of mortar, concrete and steel-fiber-reinforced concrete beams", *Cement Concrete Res.*, **30**(9), 1495-1500. https://doi.org/10.1016/S0008-8846(00)00358-6.

Xue, L., Qin, S., Sun, Q., Wang, Y., Lee, L.M. and Li, W. (2014), "A study on crack damage stress thresholds of different rock types based on uniaxial compression tests", *Rock Mech. Rock*

Eng., **47**(4), 1183-1195. https://doi.org/10.1007/s00603-013-0479-3.

Yang, D., Zhang, D., Niu, S., Dang, Y., Feng, W. and Ge, S. (2018), "Experiment and study on mechanical property of sandstone post-peak under the cyclic loading and unloading", *Geotech. Geol. Eng*., **36**(3), 1609-1620. https://doi.org/10.1007/s10706-017-0414-6.

Zhang, G., Li, H., Wang, M., Li, X., Wang, Z. and Deng, S. (2019), "Crack-induced acoustic emission and anisotropy variation of brittle rocks containing natural fractures", *J. Geophys. Eng*., **16**(3), 599-610. https://doi.org/10.1093/jge/gxz031.

Zhang, Q., Liu, C., Duan, K., Zhang, Z. and Xiang, W. (2020a), "True three-dimensional geomechanical model tests for stability analysis of surrounding rock during the excavation of a deep underground laboratory", *Rock Mech. Rock Eng*., **53**(2), 517-537. https://doi.org/10.1007/s00603-019-01927-0.

Zhang, Y., Wu, W., Yao, X., Liang, P., Sun, L. and Liu, X. (2020b), "Study on spectrum characteristics and clustering of acoustic emission signals from rock fracture", *Circ. Sys. Sig. Process*., **39**(2), 1133-1145. https://doi.org/10.1007/s00034-019-01168-0.

Zhang, Z., Hu, L., Liu, T. and Zheng, H. (2021), "Cluster and information entropy analysis of acoustic emission during rock failure process", *Geomech. Eng.*, **25**(2), 135-142. https://doi.org/10.12989/gae.2021.25.2.135.

Zhao, X.G., Cai, M., Wang, J. and Ma, L.K. (2013), "Damage stress and acoustic emission characteristics of the Beishan granite", *Int. J. Rock Mech. Min. Sci*., **64**, 258-269. https://doi.org/10.1016/j.ijrmms.2013.09.003.

Zhu, D., Jing, H., Yin, Q., Ding, S. and Zhang, J. (2020), "Mechanical characteristics of granite after heating and water-cooling cycles", *Rock Mech. Rock Eng*., **53**(4), 2015-2025. https://doi.org/10.1007/s00603-019-01991-6.

Zhukov, V.S. and Kuzmin, Y.O. (2020), "The influence of fracturing of the rocks and model materials on p-wave propagation velocity: experimental studies", *Izv. Phys. Solid Earth*, **56**, 470-480. https://doi.org/10.1134/S1069351320040102.

IC